ASTROPHYSICS

Laboratory unraveling of matter accretion in young stars

Guilhem Revet,[1,2] Sophia N. Chen,[1,2] Rosaria Bonito,[3,4] Benjamin Khiar,[5] Evgeny Filippov,[6,7] Costanza Argiroffi,[4] Drew P. Higginson,[2,8] Salvatore Orlando,[3] Jérôme Béard,[9] Marius Blecher,[10] Marco Borghesi,[11] Konstantin Burdonov,[1] Dimitri Khaghani,[12] Kealan Naughton,[11] Henri Pépin,[13] Oliver Portugall,[9] Raphael Riquier,[2,14] Rafael Rodriguez,[15] Sergei N. Ryazantsev,[7] Igor Yu. Skobelev,[6,7] Alexander Soloviev,[1] Oswald Willi,[10] Sergey Pikuz,[6,7] Andrea Ciardi,[5] Julien Fuchs[1,2]*

Copyright © 2017 The Authors, some rights reserved; exclusive licensee American Association for the Advancement of Science. No claim to original U.S. Government Works. Distributed under a Creative Commons Attribution NonCommercial License 4.0 (CC BY-NC).

Accretion dynamics in the formation of young stars is still a matter of debate because of limitations in observations and modeling. Through scaled laboratory experiments of collimated plasma accretion onto a solid in the presence of a magnetic field, we open a first window on this phenomenon by tracking, with spatial and temporal resolution, the dynamics of the system and simultaneously measuring multiband emissions. We observe in these experiments that matter, upon impact, is ejected laterally from the solid surface and then refocused by the magnetic field toward the incoming stream. This ejected matter forms a plasma shell that envelops the shocked core, reducing escaped x-ray emission. This finding demonstrates one possible structure reconciling current discrepancies between mass accretion rates derived from x-ray and optical observations, respectively.

INTRODUCTION

The accretion of matter is a process that plays a central role in varied astrophysical systems across the mass spectrum (*1*, *2*). It determines the exchange of mass, energy, and angular momentum between the accreting object and its surroundings and, eventually, the formation of planetary systems around stars. In the context of young stars, during the early stages of formation and evolution toward the main sequence phase, the final mass of the forming star is therefore determined by the accretion process. Hence, the analysis of accreting young stars and the structure by which matter settles on the star is of wide interest in the context of star and planet formation in general.

In our present understanding, referred to as the magnetospheric accretion model, matter (temperature, 2000 K; electron plasma density, 10^{11} to 10^{13} cm^{-3}) is accreted onto young stars through magnetized (B = 0.01 to 0.1 T) accretion columns that connect the surrounding material [from the envelope in the early phases or the edge of the disk in the classical T Tauri stage (*3*)] to the star's surface (*4*, *5*). Guided along the lines of the magnetic field that connects the surrounding material to the star, matter falls at free-fall velocity, that is, with a speed of the order of 500 km/s, and impacts onto the stellar chromosphere. A shock forms at the interaction between the accretion stream and the chromosphere, and the postshock plasma is heated to a few million degrees [for example, Argiroffi *et al.* (*6*)], with a preshock velocity of the order of 500 km/s and a postshock reduced speed of about 100 km/s. Therefore, excess emission of ultraviolet (UV) radiation and x-rays is expected to originate from this hot plasma. Investigating the shock structure and the high energy emission from the central star and its components (corona, accretion shocks, and jets) is crucial because this emission can influence important aspects of the star-disk system: It can alter the physical and chemical structures of the disk around the young star, with effects also on the disk's lifetime (*7*), and by itself, it can be used as a diagnostic tool to study the properties of the accreting material and the shock physics. Hence, analyzing the emission from these stars, in the x-ray band in particular, has been thought to allow insight into the accretion phenomenon (*8*, *9*) as well as into mass accretion rates [for example, Kastner *et al.* (*10*), Stelzer and Schmitt (*11*), and Curran *et al.* (*12*)].

Mass accretion rates are inferred in several ways. This can be done, for instance, through the analysis of optical observations [for example, Herczeg and Hillenbrand (*13*)], that is, by deducing the star accretion luminosity from its optical emission line's luminosities through an empirical relation, after which the mass accretion rate can be deduced from the accretion luminosity (*14*). More recently, the mass accretion rate of classical T Tauri stars (CTTSs) has been derived from their soft x-ray emission [for example, Argiroffi *et al.* (*6*), Schmitt *et al.* (*15*), and Günther *et al.* (*16*)]. For all methods, it is assumed that (i) the stream impacts the stellar surface with free-fall velocity from a distance equal to a few (typically five) times the radius of the star and (ii) the impact region is in stationary conditions, namely, the velocity, density, and temperature of the shock-heated plasma do not change in time.

Present issues with inferring mass accretion rates from observations of young stars

However, observations from CTTSs, where the accretion process is significant, show that there are significant discrepancies [for example,

[1]Institute of Applied Physics, 46 Ulyanov Street, 603950 Nizhny Novgorod, Russia. [2]LULI (Laboratoire pour l'Utilisation des Lasers Intenses)–CNRS, École Polytechnique; Commissariat à l'Energie Atomique et aux Energies Alternatives (CEA), Université Paris-Saclay; Sorbonne Universités, Universite Pierre et Marie Curie (UPMC) Paris 06, F-91128 Palaiseau cedex, France. [3]INAF (Istituto Nazionale di Astrofisica)–Osservatorio Astronomico di Palermo, Palermo, Italy. [4]Dipartimento di Fisica e Chimica, Università di Palermo, Palermo, Italy. [5]Sorbonne Universités, UPMC Paris 06, Observatoire de Paris, PSL (Paris Sciences et Lettre) Research University, CNRS, UMR 8112, LERMA (Laboratoire d'Etudes du Rayonnement et de la Matière en Astrophysique), F-75005 Paris, France. [6]National Research Nuclear University MEPhI (Moscow Engineering Physics Institute), Moscow 115409, Russia. [7]Joint Institute for High Temperatures, RAS (Russian Academy of Sciences), Moscow 125412, Russia. [8]Lawrence Livermore National Laboratory, Livermore, CA 94551, USA. [9]LNCMI (Laboratoire National des Champs Magnétiques Intenses), UPR 3228, CNRS-UGA-UPS-INSA, Toulouse 31400, France. [10]Institut für Laser- und Plasmaphysik, Heinrich-Heine-Universität Düsseldorf, D-40225 Düsseldorf, Germany. [11]Centre for Plasma Physics, Queen's University of Belfast, Belfast BT7 1NN, UK. [12]GSI (Gesellschaft für Schwerionenforschung) Helmholtzzentrum für Schwerionenforschung GmbH, 64291 Darmstadt, Germany. [13]INRS-EMT (Institut National de la Recherche Scientifique, Énergie, Matériaux et Télécommunication), Varennes, Québec, Canada. [14]CEA, DAM, DIF (Commissariat à l'Energie Atomique Energie Atomique, Direction des Applications Militaires Île de France), 91297 Arpajon, France. [15]Departamento de Fisica de la Universidad de Las Palmas de Gran Canaria, E-35017 Las Palmas de Gran Canaria, Spain.
*Corresponding author. Email: julien.fuchs@polytechnique.fr

Curran *et al.* (*12*) and Argiroffi *et al.* and (*17*)] between the observed x-ray luminosity and the predictions based on the UV-visible bands from the same object. However, we should note that of the two measurements, those based on UV emission provide the most direct estimate of the mass accretion rate and, hence, are the most accurate. Therefore, the discrepancy between the x-ray and UV measurements generally suggests that the main problem lies in the x-ray analysis method. In some systems, the discrepancy is moderate (that is, below a factor of 4; for example, Hen 3-600, TW Hya), whereas in others, the discrepancy is large (up to two orders of magnitude; for example, RU Lup, T Tau), but in all cases, the observed x-ray luminosity is lower than expected. On the basis of magnetohydrodynamic (MHD) models [for example, Sacco *et al.* (*5*), Matsakos *et al.* (*18*), Colombo *et al.* (*19*), Sacco *et al.* (*20*), Costa *et al.* (*21*), Orlando *et al.* (*24*), and Orlando *et al.* (*25*)], limited to two spatial dimensions so far, absorption of x-rays by an optically thick envelope of plasma surrounding the shocked plasma (*5*, *22*–*24*) is one of the several scenarios (*25*) that have been evoked to explain this discrepancy and the lower-than-expected observed x-ray luminosity. However, a direct observation of such an envelope is well beyond present-day observation capabilities.

Laboratory experiments to resolve the accretion dynamics in scaled conditions

An alternative approach to the investigation of astrophysically relevant plasma dynamics is through scaled laboratory experiments (*26*–*28*). With respect to the issue of accretion dynamics, as mentioned above, this requires mimicking in the laboratory accretion streams embedded in magnetic fields. Although laser-produced high-strength magnetic fields have been developed for some time (*29*, *30*), coupling quasi-static, externally applied (that is, not self-generated) magnetic fields with laser-produced plasmas has only recently become possible (*31*–*34*). To model in the laboratory the accretion columns guided along the lines of the magnetic field that connects the surrounding material to the star, we exploit here an experimental platform we have recently developed (*26*, *35*) that ensures the homogeneity of the externally applied magnetic field over a very large volume (cubic centimeters). As will be shown below, this is a key factor in allowing the present observations because it ensures that a homogeneous magnetic field (and also of high strength) exists over the scale of the accretion column impact and lateral expansion on the mimicked star surface.

Our experimental results obtained with this approach and with this setup (Figs. 1C and 2) provide the first direct evidence for the formation of a shell of dense ionized plasma enveloping the core postshock region, which is well consistent with three-dimensional (3D) MHD simulations of the laboratory experiment (Fig. 1B) and with 2D MHD-scaled astrophysical simulations (Fig. 1D). Furthermore, when postprocessing the astrophysical simulation (Fig. 3), this shell is observed to induce absorption of x-rays arising from the ionized central core, thus supporting the scenario of x-ray flux lowering by local medium surrounding the shocked region (*23*).

Setup of the laboratory experiment and scalability to the astrophysical configuration

To investigate the accretion dynamics of CTTSs in the laboratory, and as shown in Fig. 1A, we create a collimated narrow (diameter, 1 mm) plasma stream by imposing a high-strength (B_z = 20 T) external and uniform poloidal magnetic field onto an expanding plasma, ablated by a high-power laser (duration, 1 ns; 10^{13} W/cm^2) (*26*, *36*). The stream [v_{stream} = 750 km/s; 2 × 10^{18} cm^{-3}, plasma electron density; plasma electron temperature, 0.1 MK (*37*)] propagates parallel to the lines of the large-scale external magnetic field, as in the present picture of mass accretion in CTTSs, impacting onto an obstacle mimicking the high-density region of the star chromosphere (see Materials and Methods). The uniqueness of this laboratory experiment is not only in coupling laser-produced plasma with an externally applied, high-strength magnetic field but also in being fully 3D and in allowing simultaneous optical and x-ray emission measurements (see Fig. 1A). This setup differs in several notable ways from previous experiments focused on investigating radiative accretion shocks, where magnetic fields are totally absent (while the presence of the magnetic field is crucial in reproducing CTTSs observations in a realistic way), and in which the use of "shock tubes" (*38*, *39*) affects the dynamics of the constrained plasma.

As detailed in the Materials and Methods, we have verified that, between the two systems in which the accretion shock is not radiation-dominated (*38*), dimensionless scaling parameters (*40*) are similar and that the absence of relevant gravity in the laboratory does not preclude similarity because its effects will be significant only at late times (see below). Regarding the β parameter (the ratio of the plasma pressure

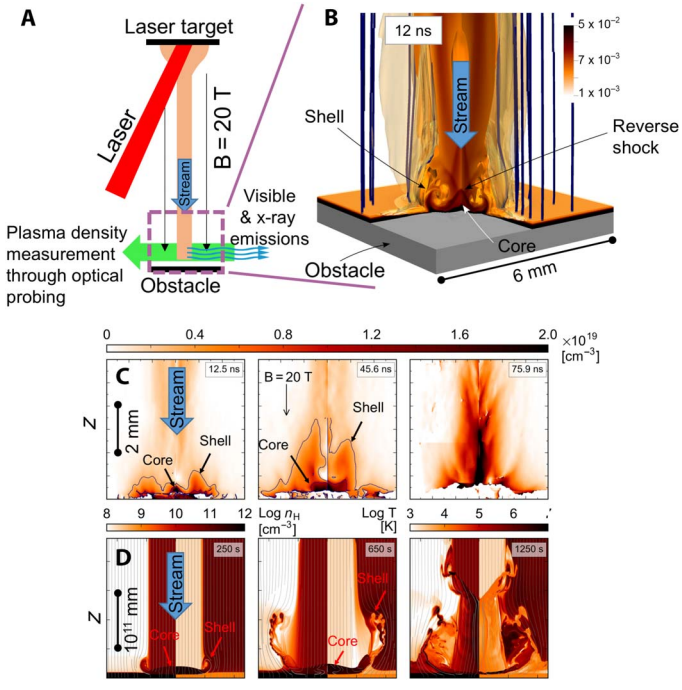

Fig. 1. Laboratory investigation of magnetized accretion dynamics and comparison with scaled astrophysical simulation of the same phenomenon highlighting the formation of a shocked core and of a surrounding shell. (**A**) Arrangement of the laboratory experiment and of the diagnostics. (**B**) Snapshot of the modeling of the laboratory experiment by the GORGON code (shown is the mass density in kg/m^3). (**C**) Measured maps, at different times (as indicated), of laboratory plasma electron density, embedded in a homogeneous and steady 20-T magnetic field. The contours displayed on the first two panels highlight the core (contour at 10^{19}cm^{-3}) and the shell (contour at 3 × 10^{18}cm^{-3}). Here, the obstacle is a CF_2 target, whereas the stream is generated from a laser-irradiated PVC $(C_2H_3Cl)_n$ target. (**D**) Simulated plasma density (left-half panels) and temperature (right-half panels) maps, also at different times, and extracted from a 2D astrophysical simulation (using the PLUTO code). In all panels, the initial magnetic field is uniform and oriented along the *z* axis; the white (resp. black) lines in (A) and (C) (resp. B) represent the magnetic field lines. In all, the obstacle/chromosphere is located at the bottom, at z = 0, and t = 0 corresponds to the moment when the stream hits the obstacle/chromosphere.

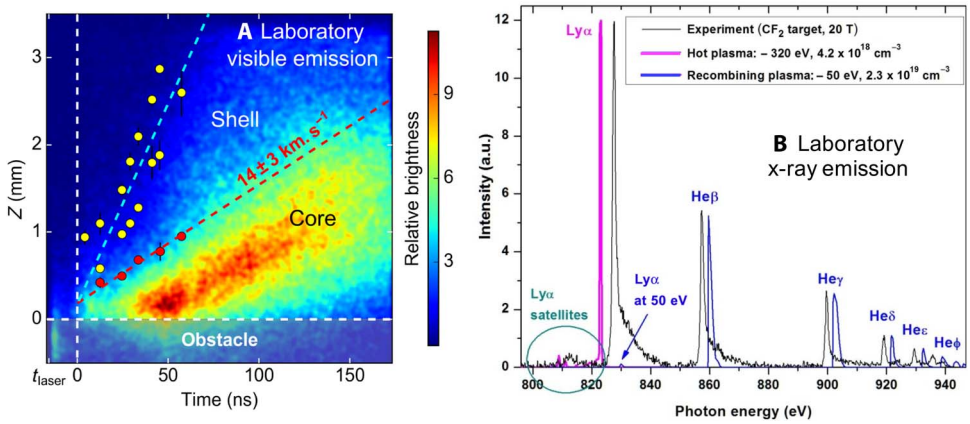

Fig. 2. Visible and x-ray emissions produced simultaneously by the shocked core and shell plasmas as recorded in the laboratory. (**A**) Visible [time- and space-resolved; here, the obstacle is a CF_2 target, whereas the stream is generated from a PVC $(C_2H_3Cl)_n$ laser-irradiated target] and (**B**) x-ray (integrated in time and in space over $0 < z < 1$ mm, that is, near the obstacle but spectrally resolved) emissions from the laboratory plasma. Note that, here, contrary to (**A**), the obstacle is a PVC $(C_2H_3Cl)_n$ target, whereas the stream is generated from a laser-irradiated CF_2 target. However, we observe that the plasma density dynamics and characteristics (density and temperature) are the same whenever the laser target and obstacle targets are swapped. In (B), the configuration using a CF_2 stream-source target is used because the spectrometer records the spectrum corresponding to the fluorine ions and that most (95 %) of the plasma seen above the obstacle is composed of stream material, as precisely analyzed by recording F-ion emissions solely originating from stream or obstacle material. The spectrum shown in (B) uses the configuration of a CF_2 stream-source target because it leads to stronger emissions compared to when using the reverse configuration of a CF_2 obstacle target. Overlaid are the simulations of the emissions produced by two plasma components having the densities of the core and shell, respectively, and temperatures of 0.58 MK (50 eV) and 3.7 MK (320 eV), respectively. Note that the modeled spectra are offset along the photon energy scale for better visibility (note also that the Ly_α line corresponds to the emission of H-like state F ions and that the He series to the emission of He-like state F ions). a.u., arbitrary unit.

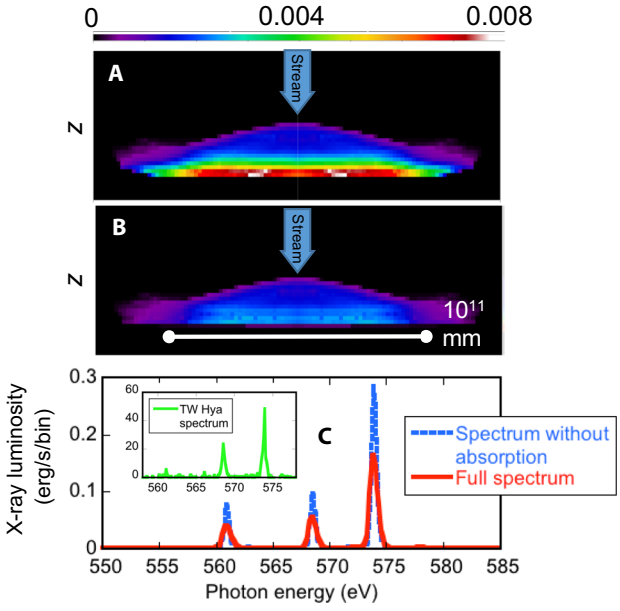

Fig. 3. Simulation of reduced x-ray emissivity from a young star due to local absorption in the shell. (**A**) Time-integrated x-ray emissivity maps (the color bar is in erg/s per grid cell) (*23*) postprocessed from the astrophysical simulation shown in Fig. 1D and looking along an axis perpendicular to the incident stream. (**B**) Same as (A) but taking into account the local absorption effect (see Materials and Methods). (**C**) The emitted spectrum, synthesized from the numerical model used for (A) and (B), in the energy range of the He-like O VII triplet and using the response function of the medium energy grating (MEG) of the Chandra satellite, with (red) and without (blue) the local absorption. Observation capabilities of maps such as (A) and (B) are unlikely, in contrast to spectra that can be directly compared with astrophysical data, such as the one shown in the inset of (C), which displays the spectrum from the CTTS TW Hydrae observed by MEG/Chandra (*9*). The unit of the ordinates of the inset is counts per bin.

to the magnetic pressure), this varies in the laboratory from <1 for the incoming stream to >1 in the shocked region (see Materials and Methods). This is imposed by the accessible laboratory conditions (lower plasma density streams are more difficult to diagnose, and higher-strength magnetic field would lead to destructive setups). These conditions are similar to what can be inferred in CTTSs when using stream densities as those typically inferred from x-ray observations (10^{11} cm^{-3}) and the lowest magnetic field values observed in CTTSs (7×10^{-4} T). Such value of magnetic field strength, is lower than expected (7×10^{-2} T). However, we stress that there is a vast variety of physical conditions that are relevant to accretion streams in CTTSs. Hence, the physical case investigated here is a representative of a class of streams with $\beta \geq 1$ and allows the unveiling of the evolution of the stream following its impact and the morphology of the postshock plasma under the strong influence of the magnetic field, notably the formation of the shell surrounding the shocked core region. In this case, the verified scaling (see Materials and Methods) between the two systems leads to the evolution of the laboratory plasma over (10 ns, 1 mm) replicating that in CTTSs over (300 s, 3×10^4 km). Note that we also varied the laboratory magnetic field strength from 6 to 30 T and, in all cases, verified the formation of a distinct dense and ionized shell around the shocked core.

RESULTS

A dense shell forms around the shocked core structure

As shown in Fig. 1 (B to D), what is observed in the laboratory and substantiated by the two MHD (in 2D and 3D) simulations (see Materials and Methods) is consistent with the following scenario: On impact, the stream, halted by the obstacle, induces the formation of an inward shock and of a reverse shock within the stream itself. The front of the reverse shock is localized by the density jump observed at

the edge of the central core in Fig. 1 (B to D). As shown in the Supplementary Materials, we verify that, in the laboratory, the increase of the plasma electron density in the core postshock region corresponds closely to what is expected from the Rankine-Hugoniot strong-shock conditions (*28*).

Simultaneously, driven by the thermal pressure, which locally overcomes the magnetic pressure ($\beta > 1$), the highly conductive and shock-heated core plasma expands radially outward, compressing and distorting the magnetic field lines (Fig. 1D, white lines). Lateral expansion is then halted by the increasing magnetic field, which redirects the plasma flow toward the stream and forms an enveloping structure that we denote here as the "shell." In Fig. 1 (B to D), we observe the ejected flow, the shell quickly overtaking (along *z*) the propagating reverse shock due to the longitudinal redirection of the ejected flow.

We stress that the plasma β of the core overwhelmingly determines the shell formation. For the regimes investigated here, radiative losses and thermal conduction play an obvious role in determining the details of the thermodynamic properties of the laboratory and astrophysical plasmas and, for example, their spectral signatures. However, as long as the core plasma β are similar (30 and 107 for the laboratory and astrophysical plasmas, respectively; see table S2), the dynamics of the formation shell is largely insensitive to these details.

We also note that the laboratory accretion streams are sustained and interact with the obstacle over a time scale that is long compared to that of the formation of the shell (that is, those shown in Fig. 1C). Nevertheless, the absence of a gravitational field capable to exert an influence on the plasma hampers our ability to experimentally reproduce the long-term dynamics of an idealized astrophysical accretion column (*25*). Instead, the experiments are limited to the initial impact and formation of the plasma shell when gravity does not have an appreciable role (which is valid for the first two frames of Fig. 1, C and D; see Materials and Methods). This is confirmed by comparing the simulations without gravity presented in our paper (Fig. 1D and movie S2) with long-term astrophysical MHD simulations that include gravity (*25*). Such comparison shows that the initial dynamics and shell formation are qualitatively similar and are largely unaffected by gravitational forces.

Our simulations do not account for radiative transfer effects, as detailed in the "Synthesis of the x-ray emission and comparison with astrophysical objects" section. This assumption can be considered valid only in the hot postshock slab and in the corona (*21*). There, the thermal conduction together with the radiative losses from optically thin plasma plays a significant role in the energy budget. In particular, the intense radiative cooling at the base of the slab robs the postshock plasma of pressure support, causing the material above the cooled layer to collapse. As a result, the shock position can vary in time (*25*). The thermal conduction acts as an additional cooling mechanism of the hot slab, draining energy from the shock-heated plasma to the chromosphere, and partially limits the growth of thermal instabilities (*25*).

On the contrary, the cold and dense material of the stream and that of the chromosphere are most likely optically thick. As a result, the radiative transfer is expected to play a significant role in the energy budget, whereas the thermal conduction should be negligible. The main effects are expected in the unshocked accretion column where the downfalling material can be radiatively heated to temperatures up to 10^5 K (*21*). Also, the optically thick material of the chromosphere and/or of the unshocked stream located along the line of sight (LoS) is expected to partially absorb the x-ray emission arising from the hot postshock slab. Note that we do not consider the effects of radiative transfer on the dynamics and energetics of the system, but we account for the absorption in the synthesis of x-ray emission, as described in the "Synthesis of the x-ray emission and comparison with astrophysical objects" section. For this reason, our modeling is not entirely self-consistent. Nevertheless, we expect that the evolution of the hot (T > 1 MK) postshock plasma is accurately modeled by radiative cooling.

Both the shocked core plasma and the shell are simultaneously observed in the recorded laboratory plasma emissivities. The reverse shock front and its temporal evolution, propagating up the stream at ~14 ± 3 km/s, are clearly seen in the streaked visible emission (see Materials and Methods) of the laboratory plasma (Fig. 2A): The reverse shock front identified in the density maps (Fig. 2A, red points) corresponds closely to the edge of the bright emitting, core postshock region that expands toward the incoming stream. In the same emission map, we can also clearly identify the shell, of reduced brightness, with its expansion front in the density maps (Fig. 1C, yellow points). Similarly, the x-ray laboratory emission originating near the obstacle surface (Fig. 2B), analyzed by our nonsteady model (*37*) and detailed in the Supplementary Information, displays features characteristic of two distinct plasma components. Here, the appearance of intense He-series lines (from emitting He-like ionized F ions) is the witness of a plasma component having a low temperature (0.6 ± 0.1 MK) at a density that corresponds well to the core density observed in Fig. 1C. The simultaneous observation of a strong Ly_α line (from emitting H-like ionized F ions) attests the presence of a higher electron temperature plasma, that is, at 3.7 MK, analyzed using the atomic code FLYCHK (*41*). This synthetic radiation, derived from the ratio between the He_β and Ly_α line intensities, has a volume and a density consistent with those of the measured shell plasma (Fig. 1C). Note that both shell and core temperatures derived this way are also well consistent with the laboratory simulation, as detailed in the Supplementary Information.

DISCUSSION

Impact of the observed shell on x-rays emitted by the shocked core

The dense and ionized shell, revealed here in the laboratory experiment and observed in the laboratory and astrophysical simulations, is seen in the latter case to modify the x-ray emission originating from the accretion region. From the x-ray emission computed from the simulation shown in Fig. 1D and comparing the results with and without local absorption effects (see Materials and Methods) taken into account (Fig. 3), we observe that the x-ray flux is significantly reduced when the local absorption is included. Thus, our results reveal that taking into account the effect of the absorption by the dense and cold shell indeed participates in the lowering of the x-ray flux that can be observed originating from such stars and, thus, influences the value of the mass accretion rate that can be inferred. The set of parameters accessible in the experiment, when scaled to the astrophysical case, corresponds to a situation where the obscuration effect (Fig. 3C) is moderate. We can expect that, for accretion streams characterized by high densities, a larger amount of optically thick material will surround the x-ray–emitting slab, inducing heavier obscuration of emitted x-rays.

Conclusion and outlook

Our results thus point to the crucial necessity to correctly account for plasma absorption to interpret and model accretion processes in young stars. Doing so allows for a more accurate, with respect to alternate scenarios, modeling of observations (*22*–*24*), thus supporting the plausibility of the dynamics highlighted here and suggesting that these conditions are

present in CTTSs. The laboratory platform developed here also opens up the investigation of a number of other issues. For example, by changing the orientation of the stream with respect to the magnetic field, alternative channels of accretion can be explored (*42*).

MATERIALS AND METHODS

Experimental design: Experiment coupling lasers and magnetic field (plasma generation)

The experiment was performed at the Equipement Laser de Forte Intensité et Energie (ELFIE) Nd:glass laser facility of the Laboratoire pour l'Utilisation des Lasers Intenses (LULI) laboratory, at Ecole Polytechnique (France) (*43*), using its chirped laser pulse, delivering 40 J of energy within a 0.6-ns full width at half maximum duration pulse at the wavelength λ = 1057 nm. This laser beam was focused on target over a 700-μm diameter flat-top spot, which gives an intensity of $I_{max} = 1.6 \times 10^{13}$ W cm^{-2}. The target was a flat solid from which, following laser irradiation, a hot plasma was created, was expanded into a vacuum, and was funneled over 3 mm into a collimated stream (*26*, *36*, *44*) by the action of a large-scale, steady poloidal external magnetic field (*35*) having a strength from 6 to 30 T, 20 T being the magnetic strength used for the results reported in the main text. The collimated plasma stream followed the magnetic field lines to hit a secondary solid target at a distance of 11.7 mm from the first target. When hitting this secondary obstacle target, the stream had a constant (over more than 100 ns) diameter of ~1.4 mm and a plasma electron density of ~1.5×10^{18} cm^{-3} when using 20 T for the magnetic field and ~1.5 mm and ~1.2×10^{18} cm^{-3} for the same quantities when using 6 T for the magnetic field, as detailed in tables S3 and S4. At 20 T, the measured plasma electron temperature was ~10 eV or 0.1 MK (*37*, *44*). We used two different materials, that is, polyvinyl chloride [PVC $(C_2H_3Cl)_n$] and Teflon (CF_2), for the two targets to be able to distinguish, through x-ray spectroscopy of the F-emitting ions (see below), the characteristics of the plasma coming from the impacting stream from the characteristics of the plasma ablated from the obstacle. These two materials were interchanged between shots between the primary and the secondary targets, that is, if the primary target is PVC, then the secondary target is Teflon and vice versa.

Both targets were situated at the center of a high-current Helmholtz coil system (*35*), constructed at the Laboratoire National des Champs Magnétiques Intenses in Toulouse (France). The Helmholtz coil was inserted inside a reentrant tube, enabling it to work at air, to allow heat dissipation and prevent any problems related to electric arcing (see also fig. S1). Two perpendicular apertures managed within the coil structure allowed free access to the laser beams propagating in the vacuum of the target chamber and allowed both targets to be inserted at the center of the coil and the diagnostics to have a free LoS to probe the plasma dynamics perpendicularly to the main axis of the stream expansion. The Helmholtz coils were coupled to a capacitor bank (32 kJ/16 kV) that delivered 20 kA to the coils to generate up to a 20-T pulsed magnetic field in the center of the coils. The current discharge in the coils took place over 204 μs (a half period of a sinusoid), and the laser irradiation was synchronized with the peak of the discharge, that is, when the magnetic field reaches its maximum strength. Hence, we can consider the magnetic field to be steady over several microseconds, which is much longer than the plasma dynamics investigated in the experiment (120 ns). The magnetic field was homogeneous in the longitudinal and radial directions over 40 mm (axially) and 20 mm (radially), respectively, which was much larger than the typical scales of the plasma dynamics (typically 12 mm axially and 5 mm radially).

Scalability between the laboratory and astrophysical plasmas

Scaling the laboratory flows to the astrophysical flows relied on the two systems described accurately enough by ideal MHD (*40*). The experiments relied on generating a relatively hot, conductive and inviscid, plasma so that the relevant dimensionless parameters are in the correct regime. Section S3 of the Supplementary Information details the respective parameters of the two plasmas. For both laboratory and astrophysical flows, respectively, in the initial conditions, that is, in the incoming stream, the Peclet number, which is the ratio of heat convection to the heat conduction, was 10 and 8×10^8, respectively; the Reynolds number, which is the ratio of the inertial force to the viscous one, was 4.6×10^5 and 2.6×10^{11}, respectively; and the magnetic Reynolds number, which is the ratio of the convection over ohmic dissipation, was 34 and 3.5×10^9, respectively. Hence, they were all $\gg 1$ for the two systems. We also quantitatively verified that the two scaling quantities determined in the study by Ryutov *et al.* (*40*), that is, the Euler

$(v\sqrt{\frac{\rho}{p}}$, where v is the flow speed, ρ is the density, and p is the pressure)

number (40.8 in the laboratory case and 87 in the astrophysical case) and the Alfven ($B/\sqrt{p}$, where B is the magnetic field) number (1.1×10^{-2} in the laboratory case and 1.2×10^{-2} in the astrophysical case), were very similar between the two systems. This ensures that both MHD systems evolved in a similar way.

The scaling of the stream radius between the experiment and the CTTS simulation, which leads to 1 mm in the experiment corresponding to 3×10^{10} mm (3×10^4 km) in the astrophysical situation, was done as follows. We used the following known quantities as a basis: stream radius (r), stream velocity (v), and stream density (ρ). Here, we used the 20-T case shown in Fig. 1C for the laboratory plasma and the ones of the PLUTO simulation shown in Fig. 1D: $r_{lab} = 0.7$ mm and $r_{astro} = 0.5 \times 10^{11}$ mm; $v_{lab} = 100$ to 1000 km/s [we measured only the 1000 km/s velocity of the detectable edge of the stream, its velocity decreasing with time as $1/t$ (*44*) and $v_{astro} = 500$ km/s]; $\rho_{lab} = 9.7 \times 10^{-6}$ g/cm^3 and $\rho_{astro} = 10^{-13}$ g/cm^3. From these, we can retrieve the following scaling factors (*40*): $a = r_{astro}/r_{lab} = 7.1 \times 10^{10}$, $b = \rho_{astro}/\rho_{lab} = 10^{-8}$, $c = v_{astro}/v_{lab} = 5$ to 0.5.

This allowed us to obtain the temporal scaling, which is $t_{astro} = (a/c) \times t_{lab}$. Hence, we can assess that, for $t > 10$ ns, when the stream velocity has dropped to ≤100 km/s, a time of 10-ns duration is equivalent to 143 s. This corresponds well to the respective temporal evolutions of the laboratory and astrophysically simulated plasmas observed in Fig. 1.

We also note that we have a good correspondence with respect to the magnetic field scaling, which is $B_{astro} = (c\sqrt{b})\, B_{lab}$. At the initial time of the impact (that is, using a stream velocity of 1000 km/s), this would yield $B_{astro} = 10^{-3}$ T for $B_{lab} = 20$ T, which corresponds well with the value 7×10^{-4} T used in the PLUTO astrophysical simulation.

We note that the magnetization of the electrons and of the ions is in good correspondence between the laboratory and astrophysical situations (see section S3 of the Supplementary Information), where in the incoming stream, ions are not magnetized, whereas the electrons are magnetized. For the rest of the dynamics, that is, after the plasma has been shocked through the impact onto the surface, both species are magnetized. One difference between the astrophysical and laboratory dynamics is, however, the thermalization time between ions and electrons. In the stream, the ions have most of the ram energy because of their mass compared to the electrons. They attain a higher gain in thermal energy through the shock by isotropization of this ram energy.

For the electrons, the temperature gain is almost negligible. The electrons can only be heated by the ions, through collisions. Regarding the density and temperature conditions reached after the shock in both cases, one can see in section S3 of the Supplementary Information that the equilibration time in the laboratory-shocked plasma is of the order of 30 ns, which was quite long compared with the time necessary for the particles to travel through the shocked region. However, in the astrophysical situation, this equilibration time was 2.5 s, which is actually negligible compared with the time necessary for the particles to travel through the shock. Consequently, in the laboratory plasma, the ion and electron temperature is decoupled during the dynamic of transit of both species, which are going through the core before being ejected out of it, to form the shell (see main text). As a consequence, in the laboratory, the electron temperature is higher in the shell than in the core. In contrast, in the astrophysical situation, the thermalization is fast enough for the electrons and ions to quickly gain the same temperature after the shock. The maximum temperature of the electrons is then already reached in the core, and the cooling by radiation leads to the temperature in the shell to be lower than in the core.

Finally, regarding the effect of the gravity, because it was absent in the laboratory experiment, we can state that, in the laboratory case, the effects of gravity on the postshock flow (and on the plasma in general) are negligible over the duration of the experiments. However, in the astrophysical context, gravitational forces are important and will tend to decelerate, over a time scale $\tau_G \sim v_{bf}/g$ (where $g = GM/R^2$ is the gravitational acceleration and v_{bf} is the characteristic speed of the backflow), the shell plasma that escapes from the shock regions and flows back along the accretion column. The time scale τ_G can be estimated by considering that the backflowing plasma was driven by the thermal energy gained in the accretion shocks. Its characteristic speed will then be of the order of the sound speed in the postshock; thus, we can write $v_{bf} \sim c_s \sim \sqrt{k_B T / \mu m_H} \sim \frac{1}{3} v_{ff}$, where for the last relation, we have used the fact that, for a strong shock, the postshock temperature is given by $k_B T \sim \frac{3}{32} \mu m_H v_{ff}^2$, where v_{ff} is the free-fall speed of the accretion flow. Thus, upon impact of the accretion flow onto the stellar surface, gravity will become important for times $\gtrsim \tau_G \sim R/(3\ v_{ff})$. As an example, for values appropriate to the CTTS MP Mus, $R = 1.3\ R_\odot$ and $M = 1.2\ M_\odot$ (*6*), this time scale is $\tau_G \sim 700$ s, which is consistent with simulations done with gravity included and with what can be seen in Fig. 1D of the main text.

Experimental diagnostics

The plasma dynamics were diagnosed using mainly four complementary diagnostics: (i) an optical diagnostic using a short-pulse laser coupled to an interferometer, allowing to measure in a snapshot the electron plasma density in the range from 5×10^{16} to 5×10^{20} cm^{-3} (*45*); (ii) a monochromatic x-ray radiography diagnostic using a short-pulse laser-driven backlighter, allowing to probe the plasma density in higher-density regions than the optical probe (*46*); (iii) a time-resolved and 1D space-resolved (along the main incoming jet and plasma expansion axis that is along the *z* axis) measurement of the plasma self-emission in the visible range, that is, exploiting streaked optical pyrometry (SOP) (*47*); and (iv) an x-ray spectrometer collecting the emission from the F-ions in the plasma to retrieve the plasma density and temperature (*37*). The first two diagnostics are 2D space and time-resolved, the third diagnostic is 1D space (along the *z* axis) and time-resolved, and the fourth diagnostic is 1D space-resolved (along the *z* axis) and time-integrated. The analysis techniques of the various diagnostics are detailed in the Supplementary Information.

Astrophysical simulations

The 2D astrophysical simulations are performed using the PLUTO code (*48*), which is a modular Godunov-type code for astrophysical plasmas. It provides a multiphysics, multialgorithm modular environment, which is detailed in the Supplementary Information, particularly oriented toward the treatment of astrophysical flows in the presence of discontinuities as in the case treated here.

The initial conditions of the simulations represent an accretion stream with constant plasma density and velocity, propagating through the stellar corona. The initial unperturbed stellar atmosphere was assumed to be magnetostatic. In detail, we adapted the wind model of Orlando *et al.* (*49*) to calculate the initial vertical profiles of mass density and temperature from the base of the transition region ($T = 10^4$ K) to the corona. Thus, the stellar atmosphere consists of a hot (maximum temperature $\approx 10^6$ K) and tenuous ($n_H \approx 2 \times 10^8$cm^{-3}) corona linked through a steep transition region to an isothermal chromosphere that is uniform at temperature (10^4 K) and is 8.5×10^8cm thick. Note that the radiative losses are set equal to zero in the chromosphere to keep it in equilibrium. Initially, the stream is in pressure equilibrium with the stellar corona and has a circular cross section with a radius $r_{str} = 5 \times 10^9$cm. We considered the case of a stream with density and velocity compatible with those derived from the analysis of the x-ray spectra of MP Mus (*6*), namely, $n_{str0} = 10^{11}$cm^{-3} and $u_{str0} = 500$ km/s at a height $z = 2.1 \times 10^{10}$cm above the stellar surface as reference; then, we considered additional simulations slightly varying the value of stream density around the reference value. The stream temperature is determined by the pressure balance across the stream lateral boundary. The unperturbed stellar magnetic field is assumed to be uniform, aligned with the stream axis, and perpendicular to the stellar surface. Because the stream impact reproduced in the laboratory experiment has an evolution that resembles that of the intermediate run By-10 in the study by Orlando *et al.* (*25*), we considered magnetic field strengths that lead to a plasma β in the postshock region similar to that of run By-10, namely, ranging from 1 to 100. For the values of the stream density explored, the magnetic field strength ranges from 7×10^{-4} to 5×10^{-3} T. Note that the values of magnetic field strength used here are slightly lower than those expected in CTTSs (see main text). However, our primary goal was to reproduce the evolution of the stream impact and the morphology of the postshock plasma observed in the laboratory experiment. Both the evolution and the morphology are guided by the plasma β value of the postshock region, which we reproduced using physical parameters as close as possible to the parameters characterizing stream impacts in CTTSs. A summary of all the simulations performed is given in section S1 of the Supplementary Information.

Synthesis of the x-ray emission and comparison with astrophysical objects

For Fig. 3, we synthesized the x-ray maps and the spectra from the D5e10-B07 model (see section S1 of the Supplementary Information). We derived both the maps and the spectra, taking into account the local absorption of the surrounding medium along the LoS or neglecting these effects. This approach allows us to infer the role of the local absorption on the detectability of the emission from the accretion shock.

The method to synthesize the maps and the spectra that can be directly compared with observations of accretion shocks consists of several steps of a tool properly developed to handle the high energy emission from shocks, as discussed in the study by Bonito *et al.* (*23*). From the bidimensional maps of the density, velocity, and temperature of the plasma simulated with the PLUTO code, we reconstructed the 3D

maps by rotating the 2D slab around the symmetry z axis (reducing the original resolution of the numerical simulations). From the values of the temperature and emission measure (EM) in each computational cell, assuming metal abundances of 0.5 of the solar values [in agreement with x-ray observations of CTTSs (*50*)], we synthesized the corresponding emission using the Chianti atomic database (*51*). We took into account the local absorption by computing the x-ray spectrum from each cell and by filtering it through the absorption column density along the LoS, that is, we took into account the emission from each cell and the absorption of each cell in front along the LoS (*23*). We used the absorption cross sections as a function of wavelength from the study by Balucinska-Church and McCammon (*52*) to compute the absorption, due mainly to cold material, as the soft x-ray opacity drops at high temperature [$T > 10^6$ K (*53*)]. We also subtracted the emission from the coronal component and neglected the absorption due to the interstellar medium. We synthesized the x-ray maps and spectra emerging from the shock region by integrating the absorbed x-ray spectra from the cells in the whole domain.

Note that our astrophysical simulations do not include the effects of radiative transfer so that they are not entirely self-consistent. However, the radiative transfer is expected to affect mostly the material of the preshock stream, developing a region of radiatively heated gas (a precursor) in the unshocked accretion column (*21*). Hence, this heating mechanism does not significantly affect the dynamics of the postshock plasma (*21*).

Simulation of the laboratory experiment using the GORGON code

The laboratory simulations of the accretion experiments were performed using the 3D resistive MHD code GORGON (*54*, *55*), a highly parallel 3D MHD code. The model describes a bi-temperature, single-fluid resistive plasma in an optically thin regime, with isotropic Braginskii-like transport coefficients. We modeled the entire experiment (as detailed in section S7 of the Supplementary Information), starting from the initial expansion of the laser-produced plasma from the first laser-irradiated target, to the impact and accretion of the collimated stream on the obstacle. The initial precursor plasma evolution, as generated by the laser irradiation (up to 1 ns), was modeled in axisymmetric, cylindrical geometry with the 2D, three-temperature, Lagrangian, radiation hydrodynamic code DUED (*56*). The laser parameters are taken to be similar to the experimental ones. The magnetic field is initially perpendicular to both laser and obstacle targets and has a magnitude of 20 T. We consider "outflow" boundary conditions for the flow and a continuous perpendicular component for the magnetic field.

SUPPLEMENTARY MATERIALS

Supplementary material for this article is available at http://advances.sciencemag.org/cgi/content/full/3/11/e1700982/DC1

Supplementary Information

section S1. Astrophysical accretion modeling using the PLUTO code

section S2. Experimental diagnostics

section S3. Comparative table of the laboratory and astrophysical plasma parameters

section S4. Temporal animation of the 2D-resolved plasma electron density measurements of the magnetized accretion of the laboratory plasma at 20 T

section S5. Temporal animation of the 2D-resolved density and temperature simulated maps of magnetized accretion dynamics in young stars

section S6. Experimental observations in the case of a 6- or 30-T applied magnetic field

section S7. Laboratory 3D MHD simulations using the GORGON code

fig. S1. Sketch of the astrophysical simulation box.

fig. S2. Radiative losses per unit EM for an optically thin plasma.

fig. S3. Cartoon showing the top view of the central coil region of the experimental setup and the diagnostics paths.

fig. S4. Shocked plasma density profiles as measured in the laboratory and simulated at the surface of a young star.

fig. S5. Illustration of the step transition observed in the transmitted x-rays between the target and vacuum or an ablated plasma expanding toward vacuum.

fig. S6. Results of the analysis of the x-ray radiographs.

fig. S7. Spectral response of the combined streak camera and filter set system used in the SOP diagnostic.

fig. S8. Best fit of the x-ray spectrum measured near the obstacle (PVC target, the stream being generated from a CF2 target) in the case of a magnetic field strength of $B = 20$ T and as obtained by the PrismSPECT code in steady-state mode for an electron temperature of 200 eV or 2.32 MK.

fig. S9. Comparison of experimental spectra (in black) recorded near the obstacle target for the cases of 20 T (left, here the obstacle is a PVC target, whereas the stream is generated from a CF2 target) and 6 T (right, here the obstacle is an Al target, whereas the stream is still generated from a CF2 target) applied B field, together with simulations (in red) of the He-like line series obtained using a recombination plasma model.

fig. S10. The spectrum measured for an applied magnetic field of 20 T (here, the obstacle is a PVC target, whereas the stream is generated from a CF2 target), in the range from 14.5 to 15.4 Å and containing the Ly_α line and its dielectronic satellites.

fig. S11. Laboratory observation of magnetized accretion dynamics using a 6-T strength for the applied magnetic field.

fig. S12. Laboratory observation of magnetized accretion dynamics for various strengths of the applied magnetic field and using a larger distance between the stream-source target and the obstacle.

fig. S13. 2D slices of the decimal logarithm of the electron density of the accretion shock region at three different times for a carbon plasma.

fig. S14. 2D slices of ion and electron temperatures as well as plasma thermal beta at $t = 22$ ns (that is, 12 ns after the stream impacts the obstacle).

table S1. Parameters for the MHD models of accretion impacts.

table S2. Parameters of the laboratory accretion, with respect to the ones of the accretion stream in CTTSs for three distinct regions, namely, the incoming stream, the score, and the shell.

table S3. Parameters, experimentally retrieved from the interferometry diagnostic, of the jet, shell, and core in the case of an applied magnetic field of 20 T.

table S4. Parameters, experimentally retrieved from the interferometry diagnostic, of the jet, shell, and core in the case of an applied magnetic field of 6 T.

movie S1. An animation of the accretion dynamics recorded as a function of time in the laboratory in the case of an applied 20-T magnetic field.

movie S2. An animation of the accretion dynamics recorded as a function of time in the astrophysical simulation (case D5e10-B07 of table S1, that is, as for Fig. 1D of the main text).

References (*57*–*82*)

REFERENCES AND NOTES

1. A. Caratti o Garatti, B. Stecklum, R. Garcia Lopez, J. Eislöffel, T. P. Ray, A. Sanna, R. Cesaroni, C. M. Walmsley, R. D. Oudmaijer, W. J. de Wit, L. Moscadelli, J. Greiner, A. Krabbe, C. Fischer, R. Klein, J. M. Ibañez, Disk-mediated accretion burst in a high-mass young stellar object. *Nat. Phys.* **13**, 276–279 (2017).
2. S. Scaringi, T. J. Maccarone, E. Körding, C. Knigge, S. Vaughan, T. R. Marsh, E. Aranzana, V. S. Dhillon, S. C. C. Barros, Accretion-induced variability links young stellar objects, white dwarfs, and black holes. *Sci. Adv.* **1**, e1500686 (2015).
3. J. Muzerolle, N. Calvet, L. Hartmann, P. D'Alessio, Unveiling the inner disk structure of T Tauri stars. *Astrophys. J. Lett.* **597**, L149–L152 (2003).
4. M. Camenzind, *Magnetized Disk-Winds and the Origin of Bipolar Outflows*, in *Accretion and Winds. Reviews in Modern Astronomy*, G. Klare, Ed. (Springer, 1990), vol. 3, pp. 234–265.
5. G. G. Sacco, S. Orlando, C. Argiroffi, A. Maggio, G. Peres, F. Reale, R. L. Curran, On the observability of T Tauri accretion shocks in the X-ray band. *Astron. Astrophys.* **522**, A55 (2010).
6. G. Argiroffi, A. Maggio, G. Peres, X-ray emission from MP Muscae: An old classical T Tauri star. *Astron. Astrophys.* **465**, L5–L8 (2007).
7. P. J. Armitage, Dynamics of protoplanetary disks. *Annu. Rev. Astron. Astrophys.* **49**, 195–236 (2011).
8. C. Argiroffi, A. Maggio, T. Montmerle, D. P. Huenemoerder, E. Alecian, M. Audard, J. Bouvier, F. Damiani, J.-F. Donati, S. G. Gregory, M. Güdel, G. A. J. Hussain, J. H. Kastner, G. G. Sacco, The close T Tauri binary system V4046 Sgr: Rotationally modulated x-ray emission from accretion shocks. *Astrophys. J.* **752**, 100 (2012).
9. N. S. Brickhouse, S. R. Cranmer, A. K. Dupree, G. J. M. Luna, S. Wolk, A deep *Chandra* x-ray spectrum of the accreting young star TW Hydrae. *Astrophys. J.* **710**, 1835 (2010).
10. J. H. Kastner, D. P. Huenemoerder, N. S. Schulz, C. R. Canizares, D. A. Weintraub, Evidence for accretion: High-resolution x-ray spectroscopy of the classical T Tauri star TW Hydrae. *Astrophys. J.* **567**, 434 (2002).
11. B. Stelzer, J. H. M. M. Schmitt, X-ray emission from a metal depleted accretion shock onto the classical T Tauri star TW Hya. *Astron. Astrophys.* **418**, 687–697 (2004).

12. R. L. Curran, C. Argiroffi, G. G. Sacco, S. Orlando, G. Peres, F. Reale, A. Maggio, Multiwavelength diagnostics of accretion in an x-ray selected sample of CTTSs. *Astron. Astrophys.* **526**, A104 (2011).
13. G.J. Herczeg, L.A. Hillenbrand, UV excess measures of accretion onto young very low mass stars and brown dwarfs. *Astrophys. J.* **681**, 594 (2008).
14. E. Gullbring, L. Hartmann, C. Briceño, N. Calvet, Disk accretion rates for T Tauri stars. *Astrophys. J.* **492**, 323 (1998).
15. J. H. M. M. Schmitt, J. Robrade, J.-U. Ness, F. Favata, B. Stelzer, X-rays from accretion shocks in T Tauri stars: The case of BP Tau. *Astron. Astrophys.* **432**, L35–L38 (2005).
16. H. M. Günther, J. H. M. M. Schmitt, J. Robrade, C. Liefke, X-ray emission from classical T Tauri stars: Accretion shocks and coronae? *Astron. Astrophys.* **466**, 1111–1121 (2007).
17. C. Argiroffi, A. Maggio, G. Peres, J. J. Drake, J. López-Santiago, S. Sciortino, B. Stelzer, X-ray optical depth diagnostics of T Tauri accretion shocks. *Astron. Astrophys.* **507**, 939–948 (2009).
18. T. Matsakos, J.-P. Chièze, C. Stehlé, M. González, L. Ibgui, L. de Sá, T. Lanz, S. Orlando, R. Bonito, C. Argiroffi, F. Reale, G. Peres, YSO accretion shocks: Magnetic, chromospheric or stochastic flow effects can suppress fluctuations of X-ray emission. *Astron. Astrophys.* **557**, A69 (2013).
19. S. Colombo, S. Orlando, G. Peres, C. Argiroffi, F. Reale, Impacts of fragmented accretion streams onto classical T Tauri stars: UV and X-ray emission lines. *Astron. Astrophys.* **594**, A93 (2016).
20. G. G. Sacco, C. Argiroffi, S. Orlando, A. Maggio, G. Peres, F. Reale, X-ray emission from dense plasma in classical T Tauri stars: Hydrodynamic modeling of the accretion shock. *Astron. Astrophys.* **491**, L17–L20 (2008).
21. G. Costa, S. Orlando, G. Peres, C. Argiroffi, R. Bonito, Hydrodynamic modeling of accretion impacts in classical T Tauri stars: Radiative heating of the pre-shock plasma. *Astron. Astrophys.* **597**, A1 (2017).
22. F. Reale, S. Orlando, P. Testa, G. Peres, E. Landi, C. J. Schrijver, Bright hot impacts by erupted fragments falling back on the sun: A template for stellar accretion. *Science* **341**, 251–253 (2013).
23. R. Bonito, S. Orlando, C. Argiroffi, M. Miceli, G. Peres, T. Matsakos, C. Stehle, L. Ibgui, Magnetohydrodynamic modeling of the accretion shocks in classical T Tauri stars: The role of local absorption in the x-ray emission. *Astrophys. J.* **795**, L34 (2014).
24. S. Orlando, R. Bonito, C. Argiroffi, F. Reale, G. Peres, M. Miceli, T. Matsakos, C. Stehlé, L. Ibgui, L. de Sa, J. P. Chièze, T. Lanz, Radiative accretion shocks along nonuniform stellar magnetic fields in classical T Tauri stars. *Astron. Astrophys.* **559**, A127 (2013).
25. S. Orlando, G. G. Sacco, C. Argiroffi, F. Reale, G. Peres, A. Maggio, X-ray emitting MHD accretion shocks in classical T Tauri stars: Case for moderate to high plasma-β values. *Astron. Astrophys.* **510**, A71 (2010).
26. B. Albertazzi, A. Ciardi, M. Nakatsutsumi, T. Vinci, J. Béard, R. Bonito, J. Billette, M. Borghesi, Z. Burkley, S. N. Chen, T. E. Cowan, T. Herrmannsdörfer, D. P. Higginson, F. Kroll, S. A. Pikuz, K. Naughton, L. Romagnani, C. Riconda, G. Revet, R. Riquier, H.-P. Schlenvoigt, I. Y. Skobelev, A.Y. Faenov, A. Soloviev, M. Huarte-Espinosa, A. Frank, O. Portugall, H. Pépin, J. Fuchs, Laboratory formation of a scaled protostellar jet by coaligned poloidal magnetic field. *Science* **346**, 325–328 (2014).
27. B. A. Remington, D. Arnett, R. P. Drake, H. Takabe, Modeling astrophysical phenomena in the laboratory with intense lasers. *Science* **284**, 1488–1493 (1999).
28. R. P. Drake, *High Energy Density Physics*, (Springer, 2006).
29. H. Daido, K. Mima, F. Miki, M. Fujita, Y. Kitagawa, S. Nakai, C. Yamanaka, Ultrahigh pulsed magnetic field produced by a CO_2 laser. *Jpn. J. Appl. Phys.* **26**, 1290 (1987).
30. C. Courtois, A. D. Ash, D. M. Chambers, R. A. D. Grundy, N. C. Woolsey, Creation of a uniform high magnetic-field strength environment for laser-driven experiments. *J. Appl. Phys.* **98**, 054913 (2005).
31. B.B. Pollock, D. H. Froul, P. F. Davis, J. S. Ross, S. Fulkerson, J. Bower, J. Satariano, D. Price, K. Krushelnick, S. H. Glenzer, High magnetic field generation for laser-plasma experiments. *Rev. Sci. Instrum.* **77**, 114703 (2006).
32. D.H. Froula, J. S. Ross, B. B. Pollock, P. Davis, A. N. James, L. Divol, M. J. Edwards, A. A. Offenberger, D. Price, R. P. J. Town, G. R. Tynan, S. H. Glenzer, Quenching of the nonlocal electron heat transport by large external magnetic fields in a laser-produced plasma measured with imaging Thomson scattering. *Phys. Rev. Lett.* **98**, 135001 (2007).
33. O. V. Gotchev, P. Y. Chang, J. P. Knauer, D. D. Meyerhofer, O. Polomarov, J. Frenje, C. K. Li, M. J.-E. Manuel, R. D. Petrasso, J. R. Rygg, F. H. Séguin, R. Betti, Laser-driven magnetic-flux compression in high-energy-density plasmas. *Phys. Rev. Lett.* **103**, 215004 (2009).
34. G. Fiksel, W. Fox, A. Bhattacharjee, D. H. Barnak, P.-Y. Chang, K. Germaschewski, S. X. Hu, P. M. Nilson, Magnetic reconnection between colliding magnetized laser-produced plasma plumes. *Phys. Rev. Lett.* **113**, 105003 (2014).
35. B. Albertazzi, J. Béard, A. Ciardi, T. Vinci, J. Albrecht, J. Billette, T. Burris-Mog, S. N. Chen, D. Da Silva, S. Dittrich, T. Herrmannsdörfer, B. Hirardin, F. Kroll, M. Nakatsutsumi, S. Nitsche, C. Riconda, L. Romagnagni, H.-P. Schlenvoigt, S. Simond, E. Veuillot, T. E. Cowan, O. Portugall, H. Pépin, J. Fuchs, Production of large volume, strongly magnetized laser-produced plasmas by use of pulsed external magnetic fields. *Rev. Sci. Instrum.* **84**, 043505 (2013).
36. A. Ciardi, T. Vinci, J. Fuchs, B. Albertazzi, C. Riconda, H. Pépin, O. Portugall, Astrophysics of magnetically collimated jets generated from laser-produced plasmas. *Phys. Rev. Lett.* **110**, 025002 (2013).
37. S. N. Ryazantsev, I. Y. Skobelev, A. Y. Faenov, T. A. Pikuz, D. P. Higginson, S. N. Chen, G. Revet, J. Béard, O. Portugall, A. A. Soloviev, A. N. Grum-Grzhimailo, J. Fuchs, S. A. Pikuz, Diagnostics of laser-produced plasmas based on the analysis of intensity ratios of He-like ions x-ray emission. *Phys. Plasmas* **23**, 123301 (2016).
38. R. P. Drake, F. W. Doss, R. G. McClarren, M. L. Adams, N. Amato, D. Bingham, C. C. Chou, C. DiStefano, K. Fidkowski, B. Fryxell, T. I. Gombosi, M. J. Grosskopf, J. P. Holloway, B. van der Holst, C. M. Huntington, S. Karni, C.M. Krauland, C. C. Kuranz, A. J. Visco, Radiative effects in radiative shocks in shock tubes. *High Energy Density Phys.* **7**, 130–140 (2011).
39. J. E. Cross, G. Gregori, J. M. Foster, P. Graham, J.-M. Bonnet-Bidaud, C. Busschaert, N. Charpentier, C. N. Danson, H. W. Doyle, R. P. Drake, J. Fyrth, E. T. Gumbrell, M. Koenig, C. Krauland, C. C. Kuranz, B. Loupias, C. Michaut, M. Mouchet, S. Patankar, J. Skidmore, C. Spindloe, E. R. Tubman, N. Woolsey, R. Yurchak, É. Falize, Laboratory analogue of a supersonic accretion column in a binary star system. *Nat. Commun.* **7**, 11899 (2016).
40. D. D. Ryutov, R. P. Drake, B. A. Remington, Criteria for scaled laboratory simulations of astrophysical MHD phenomena. *Astrophys. J. Suppl. Ser.* **127**, 465–468 (2000).
41. H.-K. Chung, M. H. Chen, W. L. Morgan, Y. Ralchenko, R. W. Lee, FLYCHK: Generalized population kinetics and spectral model for rapid spectroscopic analysis for all elements. *High Energy Density Phys.* **1**, 3–12 (2005).
42. S. Casassus, G. van der Plas, P. M. Sebastian, W. R. F. Dent, E. Fomalont, J. Hagelberg, A. Hales, A. Jordán, D. Mawet, F. Ménard, A. Wootten, D. Wilner, A. M. Hughes, M. R. Schreiber, J. H. Girard, B. Ercolano, H. Canovas, P. E. Román, V. Salinas, Flows of gas through a protoplanetary gap. *Nature* **493**, 191–194 (2013).
43. J. P. Zou, C. L. Blanc, P. Audebert, S. Janicot, A. M. Sautivet, L. Martin, C. Sauteret, J. L. Paillard, S. Jacquemot, F. Amiranoff, Recent progress on LULI high power laser facilities. *J. Phys. Conf. Ser.* **112**, 032021 (2008).
44. D. P. Higginson, G. Revet, B. Khiar, J. Béard, M. Blecher, M. Borghesi, K. Burdonov, S. N. Chen, E. Filippov, D. Khaghanil, K. Naughton, H. Pépin, S. Pikuz, O. Portugall, C. Ricondan, R. Riquier, S. N. Ryazantsev, I. Skobelev, A. Soloviev, M. Starodubtsev, T. Vinci, O. Willi, A. Ciardi, J. Fuchs, Detailed characterization of laser-produced astrophysically-relevant jets formed via a poloidal magnetic nozzle. *High Energy Density Phys.* **23**, 48–59 (2017).
45. D. W. Sweeney, D. T. Attwood, L. W. Coleman, Interferometric probing of laser produced plasmas. *Appl. Opt.* **15**, 1126–1128 (1976).
46. H.-S. Park, D. M. Chambers, H.-K. Chung, R. J. Clarke, R. Eagleton, E. Giraldez, T. Goldsack, R. Heathcote, N. Izumi, M. H. Key, J. A. King, J. A. Koch, O. L. Landen, A. Nikroo, P. K. Patel, D. F. Price, B. A. Remington, H. F. Robey, R. A. Snavely, D. A. Steinman, R. B. Stephens, C. Stoeckl, M. Storm, M. Tabak, W. Theobald, R. P. J. Town, J. E. Wickersham, B. B. Zhang, High-energy $K\alpha$ radiography using high-intensity, short-pulse lasers. *Phys. Plasmas* **13**, 056309 (2006).
47. N. C. Woolsey, C. Courtois, R. O. Dendy, Laboratory plasma astrophysics simulation experiments using lasers. *J. Phys. Conf. Ser.* **112**, 042009 (2008).
48. A. Mignone, G. Bodo, S. Massaglia, T. Matsakos, O. Tesileanu, C. Zanni, A. Ferrari, PLUTO: A numerical code for computational astrophysics. *Astrophys. J. Suppl. Ser.* **170**, 228 (2007).
49. S. Orlando, Y.-Q. Lou, R. Rosner, G. Peres, Propagation of three-dimensional Alfvén waves in a stratified, thermally conducting solar wind. *J. Geophys. Res.* **101**, 24443–24456 (1996).
50. A. Telleschi, M. Güdel, K. R. Briggs, M. Audard, L. Scelsi, High-resolution X-ray spectroscopy of T Tauri stars in the Taurus-Auriga complex. *Astron. Astrophys.* **468**, 443–462 (2007).
51. E. Landi, G. Del Zanna, P. R. Young, K. P. Dere, H. E. Mason, Chianti—An atomic database for emission lines. XII. Version 7 of the database. *Astrophys. J.* **744**, 99 (2012).
52. M. Balucinska-Church, D. McCammon, Photoelectric absorption cross sections with variable abundances. *Astron. Astrophys* **400**, 699 (1992).
53. J. H. Krolik, T. R. Kallman, Soft x-ray opacity in hot and photoionized gases. *Astrophys. J.* **286**, 366–370 (1984).
54. A. Ciardi, S. V. Lebedev, A. Frank, E. G. Blackman, J. P. Chittenden, C. J. Jennings, D. J. Ampleford, S. N. Bland, S. C. Bott, J. Rapley, G. N. Hall, F. A. Suzuki-Vidal, A. Marocchino, T. Lery, C. Stehle, The evolution of magnetic tower jets in the laboratory. *Phys. Plasmas* **14**, 056501 (2007).
55. J. P. Chittenden, S. V. Lebedev, C. A. Jennings S. N. Bland, A Ciardi, X-ray generation mechanisms in three-dimensional simulations of wire array Z-pinches. *Plasma Phys. Controlled Fusion* **46**, B457 (2004).
56. S. Atzeni, A. Schiavi, F. Califano, F. Cattani, F. Cornolti, D. Del Sarto, T.V. Liseykina, A. Macchi, F. Pegoraro, Fluid and kinetic simulation of inertial confinement fusion plasmas. *Comput. Phys. Commun.* **169**, 153–159 (2005).
57. E. Anders, N. Grevesse, Abundances of the elements: Meteoritic and solar. *Geochim. Cosmochim. Acta* **53**, 197–214 (1989).

58. V. Kashyap, J. J. Drake, PINTofALE: Package for the interactive analysis of line emission. *Bull. Astr. Soc. India* **28**, 475–476 (2000).
59. R. K. Smith, N. S. Brickhouse, D. A. Liedahl, J. C. Raymond, Collisional plasma models with APEC/APED: Emission-line diagnostics of Hydrogen-like and Helium-like ions. *Astrophys. J.* **556**, L91–L95 (2001).
60. L. Spitzer, *Physics of Fully Ionized Gases* (Interscience, 1956).
61. W. W. Dalton, S. A. Balbus, A flux-limited treatment for the conductive evaporation of spherical interstellar gas clouds. *Astrophys. J.* **404**, 625–635 (1993).
62. S. Orlando, F. Bocchino, F. Reale, G. Peres, P. Pagano, The importance of magnetic-field–oriented thermal conduction in the interaction of SNR shocks with interstellar clouds. *Astrophys. J.* **678**, 274 (2008).
63. L. L. Cowie, C. F. McKee, The evaporation of spherical clouds in a hot gas. I - Classical and saturated mass loss rates. *Astrophys. J.* **211**, 135–146 (1977).
64. J. L. Giuliani Jr., On the dynamics in evaporating cloud envelopes. *Astrophys. J.* **277**, 605–614 (1984).
65. K. J. Borkowski, J. M. Shull, C. F. McKee, Two-temperature radiative shocks with electron thermal conduction. *Astrophys. J.* **336**, 979–998 (1989).
66. Y. A. Fadeyev, H. Le Coroller, D. Gillet, The structure of radiative shock waves. IV. Effects of electron thermal conduction. *Astron. Astrophys.* **392**, 735–740 (2002).
67. T. Vinci, A. Flacco, *Neutrino* (2014); https://github.com/aflux/neutrino.
68. T. Pisarczyk, R. Arendzikowski, P. Parys, Z. Patron, Polari interferometer with automatic images processing for laser plasma diagnostic. *Laser Part. Beams* **12**, 549–561 (1994).
69. Ya. B. Zel'Dovich and Yu. P. Raizer, *Physics of Shock Waves and High-Temperature Hydrodynamic Phenomena* (New York Academic Press, 1967).
70. S. N. Chen, T. Iwawaki, K. Morita, P. Antici, S. D. Baton, F. Filippi, H. Habara, M. Nakatsutsumi, P. Nicolaï, W. Nazarov, C. Rousseaux, M. Starodubstev, K. A. Tanaka, J. Fuchs, Density and temperature characterization of long-scale length, near-critical density controlled plasma produced from ultra-low density plastic foam. *Sci. Rep.* **6**, 21495 (2016).
71. A. L. Meadowcroft, C. D. Bentley, E. N. Stott, Evaluation of the sensitivity and fading characteristics of an image plate system for x-ray diagnostics. *Rev. Sci. Instrum.* **79**, 113102 (2008).
72. S. Atzeni, J. Meyer-ter-Vehn, *The Physics of Inertial Fusion: Beam Plasma Interaction, Hydrodynamics, Hot Dense Matter* (Oxford Univ. Press, 2009).
73. A. Ya Faenov, S. A. Pikuz, A. I. Erko, B. A. Bryunetkin, V. M. Dyakin, G. V. Ivanenkov, A. R. Mingaleev, T. A. Pikuz, V. M. Romanova, T. A. Shelkovenko, High-performance x-ray spectroscopic devices for plasma microsources investigations. *Phys. Scripta* **50**, 333 (1994).
74. J. J. MacFarlane, I. E. Golovkin, P. Wang, P. R. Woodruff, N. A. Pereira, SPECT3D – A multi-dimensional collisional-radiative code for generating diagnostic signatures based on hydrodynamics and PIC simulation output. *High Energy Density Phys.* **3**, 181–190 (2007).
75. D. D. Ryutov, R. P. Drake, J. Kane, E. Liang, B. A. Remington, W. M. Wood-Vasey, Similarity criteria for the laboratory simulation of supernova hydrodynamics. *Astrophys. J.* **518**, 821 (1999).
76. M. Dorf, *Viscosity of a multispecies plasma containing hydrogen and high-Z ions* (2014); https://arxiv.org/abs/1408.3677.
77. R. S. Sutherland, M. A. Dopita, Cooling functions for low-density astrophysical plasmas. *Astrophys. J. Suppl. Ser.* **88**, 253–327 (1993).
78. J. D. Huba, *NRL Plasma Formulary* (Naval Research Laboratory, 1998).
79. L. Mejnertsen, J. P. Eastwood, J. P. Chittenden, A. Masters, Global MHD simulations of Neptune's magnetosphere. *J. Geophys. Res. Space Physics* **121**, 7497–7513 (2016).
80. D. Salzmann, *Atomic Physics in Hot Plasmas* (Oxford Univ. Press, 1998).
81. E. M. Epperlein, M. G. Haines, Plasma transport coefficients in a magnetic field by direct numerical solution of the Fokker–Planck equation. *Phys. Fluids* **29**, 1029 (1986).
82. S. I. Braginskii, Transport processes in plasma, in *Reviews of Plasma Physics*, M. A. Leontovich, Eds. (Consultants Bureau, 1965), vol. 1, p. 205.

Acknowledgments: We thank the LULI teams for technical support, the Dresden High Magnetic Field Laboratory at Helmholtz-Zentrum Dresden-Rossendorf for the development of the pulsed power generator, B. Albertazzi and M. Nakatsutsumi for their previous work in laying the groundwork for the experimental platform, and P. Loiseau for the discussions. **Funding:** This work was supported by ANR Blanc grant no. 12-BS09-025-01 SILAMPA (France) and by the Ministry of Education and Science of the Russian Federation under contract no. 14.Z50.31.0007. This work was partly done within the Plas@Par LABEX project and supported by grant 11-IDEX- 0004-02 from ANR (France). The JIHT RAS (Joint Institute for High Temperatures Russian Academy of Sciences) and National Research Nuclear University (NRNU) Moscow Engineering Physics Institute (MEPhI) members acknowledge the support of the Russian Foundation for Basic Research (RFBR) foundation under the framework of projects #14-29-06099 and #15-32-21121 and the Competitiveness Program of NRNU MEPhI. O.W. would like to acknowledge the German Research Foundation Programmes GRK 1203 and SFB/TR18. M. Borghesi and K.N. acknowledge funding from the Engineering and Physical Sciences Research Council (grants EP/J500094/1 and EP/P010059/1). A.C., S.O., R.B., and C.A. acknowledge the support of Projet International de Coopération Scientifique PICS 6838 of CNRS. Part of the experimental system is covered by a patent [no. 1000183285, 2013, Institut National de la propriété industrielle (INPI), France]. PLUTO is developed at the Turin Astronomical Observatory in collaboration with the Department of Physics of Turin University. A.S. acknowledges funding from the RFBR foundation under the framework of projects #16-32-60183. Part of this work was supported by the region Ile-de-France through the program Domaine d'Intérêt Majeur Astrophysique et Conditions d'Apparition de la vie (DIM) ACAV. R.B. acknowledges the support of the Istituto Nazionale di Astrofisica (INAF) under the PRIN2013 Programme "Disks, jets and the dawn of planets." This work was performed under the auspices of the U.S. Department of Energy by Lawrence Livermore National Laboratory under Contract DE-AC52-07NA27344. **Author contributions:** J.F. and A.C. designed the project. J.F., D.P.H., and J.B. designed the experiment. J.B. and O.P. designed the pulsed high-magnetic field system. G.R., S.P., E.F., D.P.H., S.N.C., J.F., J.B., K.N., M. Blecher, K.B., A.S., D.K., H.P., and R. Riquier performed the experiment, with M. Borghesi and O.W. providing support. G.R., S.N.C., S.P., E.F., S.N.R., I.Y.S., and J.F. analyzed the laboratory data. S.O., C.A., R. B., B.K., R. Rodriguez, and A.C. designed and performed the simulations. J.F., G.R., S.N.C., S.O., C.A., R.B., S.P., A.C., and B.K. wrote the article. All the authors provided comments on the various stages of the article. **Competing interests:** J.F., O.P., J.B., and H.P. are authors on a patent related to this work issued by the INPI, France (no. 14710032.5, 27 Feb 2013). The authors declare that they have no other competing interests. **Data and materials availability:** All data needed to evaluate the conclusions in the paper are present in the paper and/or the Supplementary Materials. The experimental data and simulations are, respectively, archived on servers at the LULI, LERMA (Laboratoire d'Etudes du Rayonnement et de la Matière en Astrophysique), and INAF laboratories and can be consulted upon request.

Submitted 28 March 2017
Accepted 5 October 2017
Published 1 November 2017
10.1126/sciadv.1700982

Citation: G. Revet, S. N. Chen, R. Bonito, B. Khiar, E. Filippov, C. Argiroffi, D. P. Higginson, S. Orlando, J. Béard, M. Blecher, M. Borghesi, K. Burdonov, D. Khaghani, K. Naughton, H. Pépin, O. Portugall, R. Riquier, R. Rodriguez, S. N. Ryazantsev, I. Yu. Skobelev, A. Soloviev, O. Willi, S. Pikuz, A. Ciardi, J. Fuchs, Laboratory unraveling of matter accretion in young stars. *Sci. Adv.* **3**, e1700982 (2017).